JOURNAL OF SPACECRAFT AND ROCKETS
Vol. 29, No. 5, September-October 1992

Calculated Electron Number Density Profiles for the Aeroassist Flight Experiment

Robert B. Greendyke*
ViGYAN, Inc., Hampton, Virginia 23666
and
Peter A. Gnoffo† and R. Wes Lawrence‡
NASA Langley Research Center, Hampton, Virginia 23665

Basic features of a Microwave Reflectometer Ionization Sensor (MRIS) as designed for use on the Aeroassist Flight Experiment are described. The MRIS is designed to measure the distances into the shock layer of four critical electron number densities corresponding to four frequencies (20, 44, 95, and 140 GHz). A parametric study of the effects of trajectory and several thermochemical nonequilibrium models for reaction rates, translational and vibrational-electronic energy exchange rates, the average electronic excitation level of atoms, and axisymmetric vs three-dimensional effects is conducted for evaluating MRIS contributions to the code validation process. The parametric study, implemented with the Langley Aerothermodynamic Upwind Relaxation Algorithm program, reveals a particular sensitivity of the onset and severity of an electron avalanche phenomena associated with changes in these physical models that lead to strong electron-impact ionization. Predicted electron number density profiles are sensitive to reasonable variations in certain kinetic models; consequently, MRIS measurements could assist the code validation process.

Nomenclature

a = thermal exponent, usually equal to 0.3
b = thermal exponent, $1 - a$
f = frequency, GHz
$\hat{I}$ = ionization potential energy, eV
N_c = critical number density, cm^{-3}
T = heavy particle translational temperature, K
T_{ave} = average temperature, K
T_V = electron translational and heavy particle vibrational temperature, K
t = time, s
σ_V = limiting vibrational excitation cross section, m^2

Introduction

THE Aeroassist Flight Experiment[1] (AFE) is a project designed to obtain critical flight data that has a number of objectives, including the validation of computational fluid dynamic (CFD) simulation methods of hypersonic flows in thermochemical nonequilibrium. One important element in the assembly of experiments on the AFE is the Microwave Reflectometer Ionization Sensor (MRIS). The MRIS sits just below the inner vehicle mold line (Fig. 1) beneath the stagnation region of the flowfield and transmits and receives microwaves through the thermal protection system (TPS) tiles. The MRIS will provide direct measurements of critical electron number densities in the plasma sheath surrounding the AFE (Fig. 2) and indirect measurements of the distance from the body surface to the critical electron number densities (Fig. 3) in the thermochemical nonequilibrium environment. The purpose of the present work will be to investigate how uncertainties in some of the physical models impact the electron number density profiles calculated for the shock layer of the AFE, and how these models influence the anticipated results of the MRIS experiment.

The detailed discussion of the propagation of electromagnetic waves within the plasma and the resultant coupling between apertures is beyond the scope of this work, but may be found in Refs. 2 and 3. A simple explanation is that the electromagnetic wave can be assumed to reflect from the plasma sheath at the point where the electron number density equals $N_c(f)$; that is, where the plasma is in resonance with the electromagnetic wave. For the four MRIS channels, the critical number densities in cm^{-3} are approximately $N_c(20) = 4.96 \times 10^{12}$, $N_c(44) = 2.40 \times 10^{13}$, $N_c(95) = 1.12 \times 10^{14}$, and $N_c(140) = 2.43 \times 10^{14}$. The electromagnetic wave for each channel will be reflected when the electron number density reaches N_c for that channel as shown in Fig. 3.

The MRIS must measure the time required for a pulse at each channel frequency to travel to the corresponding critical number density and from this measurement infer a distance.

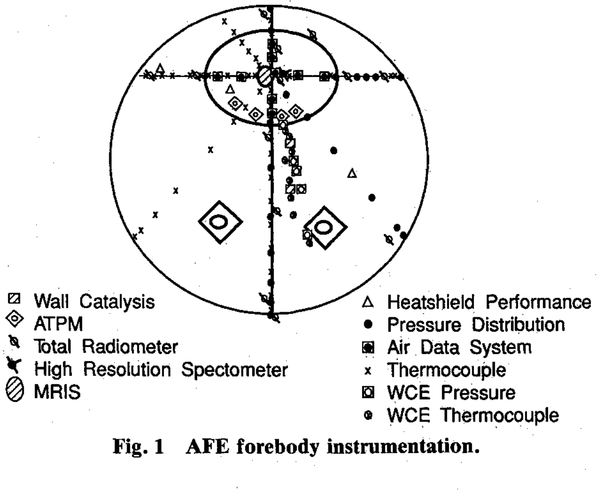

Fig. 1 AFE forebody instrumentation.

Received Dec. 2, 1991; presented as Paper 92-0804 at the AIAA 30th Aerospace Sciences Meeting, Reno, NV, Jan. 6-9, 1992; revision received Feb. 19, 1992; accepted for publication Feb. 21, 1992.

*Research Engineer. Member AIAA.

†Aerospace Engineer, Aerothermodynamics Branch, Space Systems Division. Associate Fellow AIAA.

‡Aerospace Engineer, Antenna and Microwave Research Branch, Guidance and Control Division.

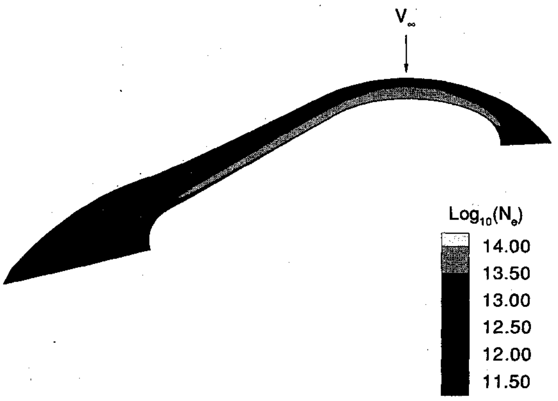

Fig. 2 Typical electron number density contours on AFE symmetry plane.

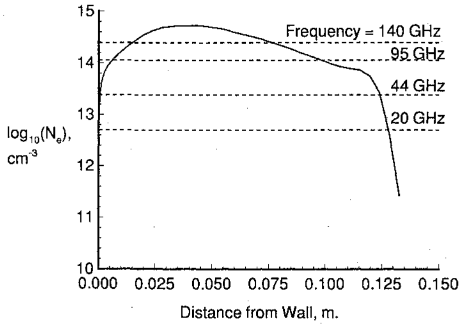

Fig. 3 MRIS critical electron number densities.

The instrument records the reflection or coupling coefficient at 64 individual frequencies separated by 64 MHz about the center frequency of each channel. The Fourier transform of these measurements can then be used to synthesize a pulse at each channel frequency.

The time delay for this pulse to travel to the plasma and return is then measured, and thus, a distance traveled for the pulse for an assumed velocity can be obtained. Since the presence of free electrons effects microwave pulse velocity, an assumed electron density profile shape between measurement frequencies is then used to estimate the pulse velocities throughout the plasma sheath. Using this assumed velocity, the estimated distances to the critical number densities, and thus the estimated electron number density profile, can be obtained.

The delay measurement will be performed using the reflection coefficient for the 20-GHz channel and the coupling coefficient for the three higher frequency channels. This inferred profile measurement will be made five times per second during the aeropass. In addition, at two times during the aeropass, a 1-s burst mode will be implemented, and the profile measurement will be made at 100 Hz for 1 s. A complimentary diagnostic technique is also possible, whereby the predicted reflected signal based on a predicted electron number density profile can be compared to the measured reflected signal. Additional instrument details can be found in Refs. 2 and 3.

Several difficulties are associated with the inversion of time delays to distances. First, due to the limited bandwidth at each channel, resolution and differentiation of reflections from the TPS tile and from the plasma is limited. Therefore, more complex methods must be used to reduce measurement error due to TPS reflections. In addition, since the measurement error is strongly dependent on the assumed functional form for the electron number density between measurement frequencies, the determination of the appropriate assumed form is extremely important. Finally, transmission properties through the tile at elevated temperatures, particularly at temperatures above 2700°F when the reactive cured glass (RCG) tile coating begins to soften, are unknown.

The difficulties in obtaining these measurements are offset by their value in the CFD code validation process when coupled with the other experimental measurements made simultaneously on the AFE. The MRIS provides the only nonintrusive profile characterization of the flowfield surrounding the AFE which shows sensitivity to the details of the physical models. (Radiation measurements on the AFE are nonintrusive but provide only integrated profile information.) This study investigates the effects of representative kinetic model and trajectory parameters on predicted electron number density profiles across the AFE shock layer. Furthermore, it examines the ability of the MRIS experiment to provide a means of differentiating between the appropriateness of the various kinetic parameters. Obviously, all of the possible permutations and combinations of physical models and trajectory points have not been tested here. Errors in one aspect of the modeling may compensate for errors made in some other aspect. It is unlikely that such compensation will exactly balance over an entire trajectory, but even this possibility cannot yet be ruled out. Consequently, the MRIS experiment cannot be used in and of itself to validate any single kinetic model used in the simulation. However, the code validation process requires several different kinds of measurements that exhibit sensitivity to unknowns in the physical modeling. The ability of the MRIS measurement to contribute to this validation process is therefore an important consideration in this paper.

Finally, we note that, due to budget constraints, the realization of an AFE flight at any time in the future is uncertain. The specific program that supported this work has been cancelled. This study, therefore, serves an additional purpose of documenting the currently known capabilities and limitations of the MRIS as it relates to flowfield diagnostics so that it may be considered in the design of future flight experiments.

Overview

Several phenomena have a direct influence on the electron number density. Thermochemical nonequilibrium models for reaction rates, translational and vibrational-electronic energy exchange rates, the average electronic excitation level of atoms, and axisymmetric vs three-dimensional effects all have a large impact on the electron number density profiles.

The chemical reaction rates are nontrivial functions of their nonequilibrium thermal state. This functionality is empirically modeled using a rate controlling temperature T_{ave},

$$T_{\text{ave}} = T_V^a \times T^b \tag{1}$$

in Park's two temperature model.[4] A baseline specification of $a = 0.3$ and $b = 0.7$ was used in the present work. The chemical kinetic models of both Park[5,6] and Kang and Dunn[7] have been included in the parametric study.

The vibrational-electronic energy equation must account for the vibrational energy lost through dissociation and the electron translational energy lost through the process of electron impact ionization. [See terms 8 and 9 of Eq. (16) in Ref. 8. Equation (52) of Ref. 8 has also been modified to account for the deionization rate in the present study.] The vibrational energy loss term is modeled using the average vibrational energy of the system, thus assuming that the effects of preferential dissociation of vibrationally excited molecules are minimal. There is no parametric variation of this model included here. In modeling the electron translational energy lost in impact ionization, it is assumed that the freed electron comes either from the ground electronic state or the first excited state. This model has a direct impact on the magnitude of T_V. The rate controlling temperature for electron impact ionization reactions throughout this study is T_V.

A more indirect, yet nonetheless significant, parameter to study is the empirically defined, high-temperature limit for vibrational-translational energy exchange cross section σ_V.[4] The value of σ_V determines the rate of relaxation of the vibrational energy, which directly impacts the level of ionization at temperature above 8000 K, where the Millikan and White theory yields inappropriately large cross sections (see Eq. (56) of Ref. 8). All of these parameters will be examined in this study as they apply to the AFE and the AFE's MRIS experiment.

The effects of coupled, radiative energy transfer on the electron number density profiles are not documented in this study. Preliminary calculations show that radiative cooling tends to lower the vibrational-electronic temperature across the shock layer, thus diminishing the electron-impact ionization rates and lowering the electron number density. However, the nonequilibrium radiation models and the coupling algorithm require further evaluation and testing and were judged to be insufficiently developed to be included in this study.

Method

The Langley Aerothermodynamic Upwind Relaxation Algorithm (LAURA) code[8,9] was used throughout this study for the simulation of AFE flowfields in both axisymmetric and three-dimensional fashion. The LAURA code is a point-implicit relaxation algorithm for obtaining the numerical solution to the governing equations for viscous hypersonic flows in chemical and thermal nonequilibrium. The algorithm is derived using a finite volume formulation in which the inviscid components of the flux across cell walls are described with Roe's averaging[10] and Harten's entropy fix[11] with second-order corrections based on Yee's symmetrical total variation diminishing scheme.[12,13]

The code includes 11 species continuity equations, three momentum equations, and one energy equation each for both the vibrational-electronic and total energies. The vibrational and electronic energies of all species are assumed to be in equilibrium at a temperature T_V, and the translational and rotational energies in equilibrium at temperature T_H. Stewart's finite rate catalytic wall boundary condition[14] was incorporated into the solution routine for all cases. As noted earlier, radiative heat transfer was not included in this study.

Kinetic and Geometric Model Variations

In the first part of this investigation, we will consider the variation of three main kinetic model parameters and their influence on the electron number densities along the stagnation streamline of the AFE. The first, identified by the letter I, is the reference value of ionization potential $\hat{I}$. The number following I in the case identifier denotes which set of reference values were used. The primary ($I = 1$) set of ionization potentials represents the energy required to ionize an atom from an already excited state, whereas the secondary ($I = 2$) set of potentials are the ionization potentials measured from the ground state of the given species. Thus, $\hat{I}(N) = 4.196$ eV and $\hat{I}(O) = 4.453$ eV for $I = 1$ and $\hat{I}(N) = 14.53$ eV and $\hat{I}(O) = 13.614$ eV for $I = 2$.

The second parameter varied is the choice of chemical rates and is identified by K. The choices, in numerical order from $K = 1$-5, are 1) the rates of Kang and Dunn,[7] 2) the rates used by Park in 1987,[5] 3) Park's rates from 1990,[6] 4) Kang and Dunn's forward rates with Gupta's equilibrium constant,[15] and finally, 5) Park's rates from 1990 with Gupta's equilibrium constant.

The final parameter, identified by S, is the value of the limiting cross section for vibrational excitation. The first option ($S = 1$) is the curve fit value of Park,[4] where

$$\sigma_V = 1 \times 10^{-17} \left(\frac{50{,}000}{T}\right)^2 \tag{2}$$

The second option ($S = 2$) is a constant value of the limiting cross section

$$\sigma_V = 1 \times 10^{-16} \tag{3}$$

The third option ($S = 3$) is another constant value of the limiting cross section

$$\sigma_V = 1 \times 10^{-17} \tag{4}$$

The $S = 2$ and 3 options roughly bound the expression given in Eq. (2). When varying the three main kinetic model parameters, all cases were solved using the axisymmetric version of LAURA at point 2 of a typical AFE trajectory listed in Table 1. The computational grid utilized in all solutions for this section had 64 cells in the direction normal to the body and 32 cells along the surface of the body.

The version of the LAURA code used for this study has two body geometry options available. The first option is the full three-dimensional AFE body. The second option is an equivalent sphere with a nose radius that yields the same stagnation point convective heating as the true AFE. The parametric study was implemented on the sphere for reasons of computational economy. In order to determine the effects of body geometries on electron number density profiles, the LAURA code was used to simulate the forebody flowfield over an equivalent sphere with a nose radius of 2.16 m at point 1 on the AFE trajectory. This simulation allowed comparison with three-dimensional data obtained from a previous study conducted on the true AFE shape at that point with the baseline values: $I = 1$, $K = 2$, and $S = 1$. The grid utilized for the three-dimensional solution had 21 cells circumferentially, 42 longitudinally, and 64 cells in the normal direction.

Trajectory Point Variations

In the second portion of this study, a parametric study was done wherein the altitude was varied along a second typical AFE trajectory while the kinetic model parameters were held fixed. The trajectory used was designated by NASA as the Baseline V trajectory, and points of it used in this work are represented by points 3-12 in Table 1. The times presented in the table represent time from entry interface with the Earth's atmosphere.

Updates in the baseline kinetic model were included in this portion of the study. The new version, following the suggestion of Hansen,[16] replaces the exponents in Eq. (1) with

$$a = [0.1 + 0.4 \times (T_V/T)] \tag{5}$$

and

$$b = [0.9 - 0.4 \times (T_V/T)] \tag{6}$$

In addition, the species number density used in Eq. (56) of Ref. 8 was changed to the total number density to better reflect true collisional probabilities. These code updates made quantitative differences in the flowfield solutions from the previous section. The differences can be seen by comparing results from the earlier model at trajectory point 2 with results from the updated model at the similar trajectory point 4. The other kinetic model parameters in the solution method, examined in the first section, were held constant at the baseline (I1K2S1) values while the freestream conditions varied from

Table 1 Trajectory points

Point	Time, s	Altitude, km	Velocity, km/s	Density kg/m^3	Temperature, K
1	—	81.32	9.818	1.542×10^{-5}	195.3
2	—	78.46	9.688	2.484×10^{-5}	197.3
3	70	82.96	9.848	1.160×10^{-5}	193.9
4	90	78.72	9.683	2.347×10^{-5}	197.1
5	110	76.47	9.418	3.412×10^{-5}	198.5
6	130	75.40	9.086	4.071×10^{-5}	199.3
7	150	75.03	8.744	4.323×10^{-5}	199.5
8	170	75.28	8.420	4.151×10^{-5}	199.3
9	190	76.15	8.415	3.595×10^{-5}	198.7
10	210	77.73	7.930	2.765×10^{-5}	197.7
11	230	79.98	7.778	1.904×10^{-5}	196.3
12	250	82.53	7.678	1.246×10^{-5}	194.2

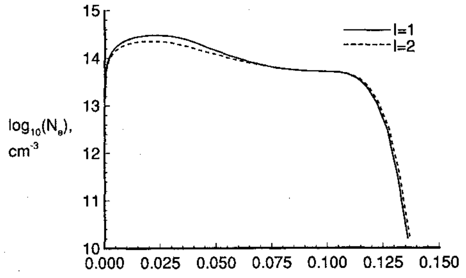

a) Variation with ionization potential

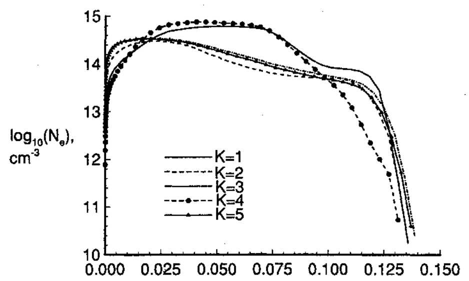

b) Variation with kinetic model

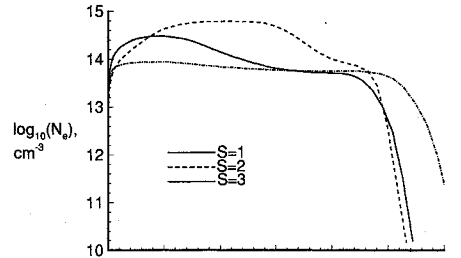

c) Variation with σ_V

Fig. 4 Electron number density profile at point 2.

point 3 to point 12 of the trajectory in Table 1. The grid used for the trajectory variations had 30 cells circumferentially and 128 cells in the normal direction.

Results

Kinetic and Geometric Model Variations

Examination of Fig. 4a indicates that, when the reference value of the ionization potential was allowed to vary, the highest rate of ionization was seen where ionization was assumed to be taking place from an already excited state. This result conforms to expected patterns for the I1K2S1 and I2K2S1 cases since there is less of a drain on the vibrational-electronic energy pool for the $I = 1$ option, thus raising the vibrational temperature relative to the $I = 2$ option. The higher vibrational temperature enhances the electron impact ionization rates, which are a function of T_V. In both cases, the electron number density peaks approximately 2.5 cm from the wall. Note that there would be no reflection from the 140-GHz frequency for the $I = 2$ case, but there would be reflection for the $I = 1$ case.

In Fig. 4b, it is seen that the choice of chemical rates has a strong influence on the electron number density. The K = 1 and 4 (Kang and Dunn rates) produce the largest electron number densities. It is interesting to note the dual plateau in the $K = 1$ case. The magnitude of the electron number density, as well as the dual plateau effect, are attributed to an electron avalanche effect caused by the onset of electron impact ionization as an important kinetic mechanism once a critical electron number density is achieved. (See the section titled Avalanche Ionization in Chap. 5 of Ref. 6). The K = 2, 3, and 5 cases (Park rates) also manifest a lesser electron avalanche that is delayed until farther into the shock layer. The ability of the MRIS to return distances of critical number densities in the shock layer might be used to help understand which mechanism is more accurate.

The variation of the limiting cross section for vibrational excitation is shown in Fig. 4c. The $S = 2$ case, which uses the largest limiting cross section of the three possible parameters, produced the largest degree of ionization. This behavior corresponds to a more efficient transfer of translational energy into the vibrational-electronic modes, which in turn enhances ionization rates. There is also a dual plateau profile suggesting an electron avalanche effect.

The $S = 3$ option produces the smallest degree of ionization while on the average having the smallest cross section. An electron avalanche effect is not indicated in this case and there was a significant increase in the shock layer thickness due to the retardation of reaction rates as a function of the lower values for T_{ave}.

The $S = 1$, or curve-fit value of the cross section, yielded the expected dual plateau pattern with the second plateau delayed until well into the shock layer.

The effect of the empirical modeling of σ_V on shock layer profiles is significant and needs careful scrutiny in the design of validation experiments. The MRIS measurements would be sensitive to these variations in both magnitude and location of the peak electron number density.

The differences in electron number density between axisymmetric and three-dimensional solution methods appears to be minimal. Examination of Fig. 5 indicates that, aside from the increased thickness of the shock layer due to three-dimensional effects, electron densities are similar for the two I1K2S1 cases. The slight increase in electron densities for the three-dimensional case is probably due to the increased time for reaction within the thicker shock.

Trajectory Point Variations

As altitude is varied in Figs. 6a–j, several interesting patterns emerge. In Fig. 6a, the maximum altitude and velocity for this study is considered. The peak heavy particle temperature is the highest of the cases due to the vehicle's velocity, and the nonequilibrium region of the flowfield is large in depth at this point as is the shock layer as a whole. Because of the high temperatures in the immediate postshock region, initial ionization is rapid. In Fig. 6a, the initial high rate of ionization is followed by a second region wherein ionization has a rapid pulse due to the electron avalanche effect. The process declines only as the boundary layer is entered.

As the vehicle's velocity and altitude decrease, Figs. 6b–d, the magnitude of the electron avalanche declines. The nonequilibrium region decreases thickness as the thermal profiles become more defined. The heavy particle temperature decreases from approximately 31,000 to 28,000 K, while the peak vibrational-electronic temperature remains fairly constant at 12,000 K. All electron number density profiles peak at 1.5–2 cm from the wall, while getting progressively flatter.

Reflections from all four MRIS frequencies would be expected in this range, though the 140-GHz reflection point is borderline at $t = 130$ s. It would be sometime during this period that the peak heating would occur and the radiative

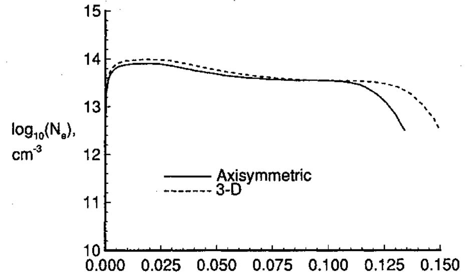

Fig. 5 Electron number density profile at point 1.

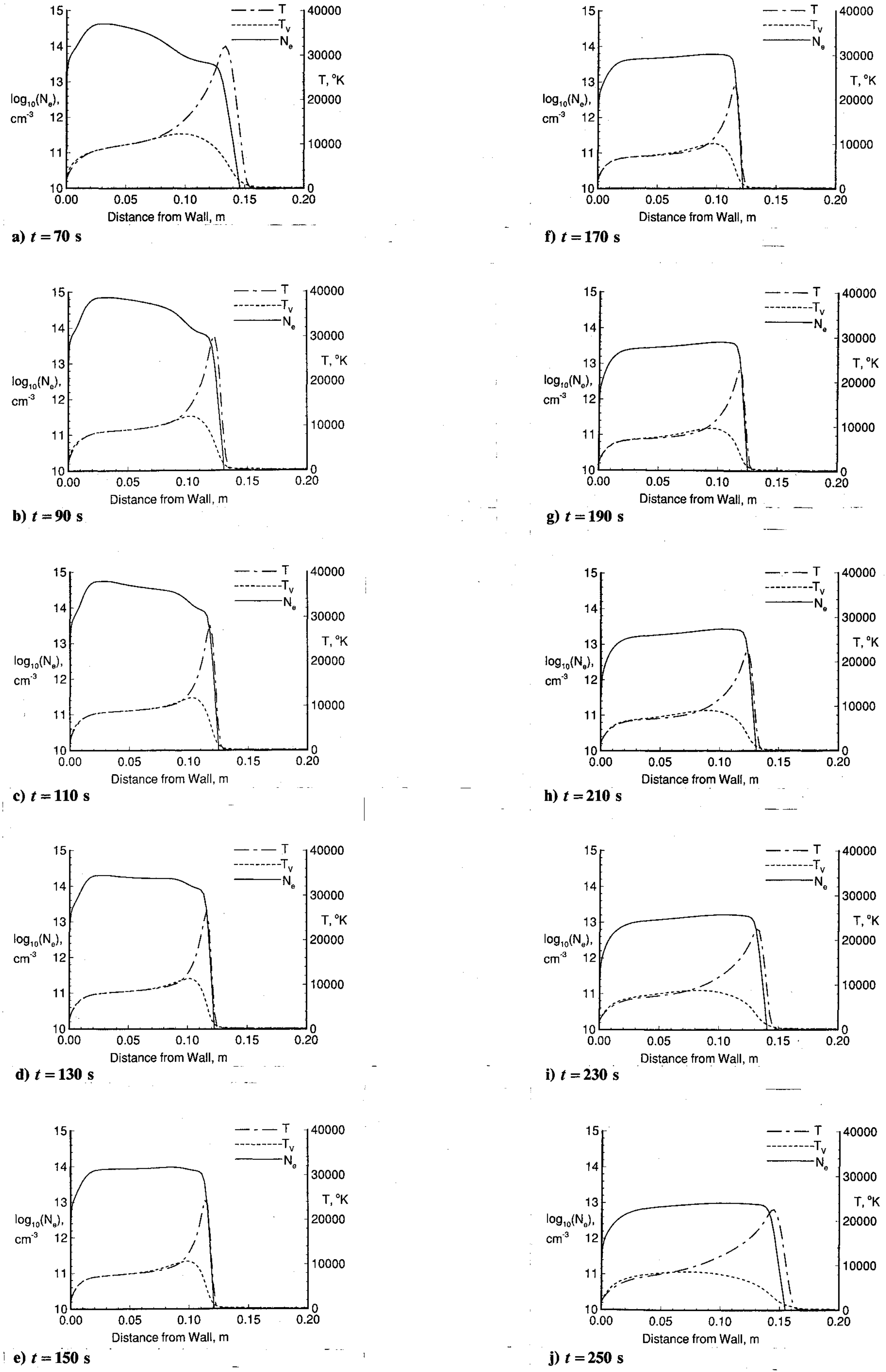

a) $t = 70$ s

b) $t = 90$ s

c) $t = 110$ s

d) $t = 130$ s

e) $t = 150$ s

f) $t = 170$ s

g) $t = 190$ s

h) $t = 210$ s

i) $t = 230$ s

j) $t = 250$ s

Fig. 6 Stagnation streamline profiles.

equilibrium wall temperature may be high enough to soften the RCG tile coating, possibly jeopardizing MRIS transmission capability through the tile. Validation data for kinetics associated with the onset of the avalanche effect would be lost if the tile becomes opaque to high frequency waves during this time.

In Fig. 6e, at 150 s into the trajectory, the lowest altitude case for this study is presented. At this point, the electron avalanche effect is barely visible. Peak electron number density is at approximately 9 cm from the wall, although difficult to observe due to the flatness of the profile. The peak value is below the maximum critical number density perceptible at 140 GHz by the MRIS experiment and remains so throughout the remainder of the trajectory considered here. The shock layer thickness and nonequilibrium region depth are at their minimum. Vibrational-electronic temperatures have declined only slightly, with a peak value of approximately 10,000 K.

By 170 s into the AFE trajectory, the vehicle has begun to exit the atmosphere. Peak heavy particle temperature in Fig. 6f has declined to approximately 24,000 K, and the peak vibrational-electronic temperature is holding at 10,000 K. There is no longer a clearly defined region wherein the electron-impact ionization can be said to dominate the ionization reactions. It appears that the threshold level of electron number density necessary for an electron avalanche effect to occur is not reached.

As the AFE continues its ascent, the nonequilibrium region of the flow continues to grow in depth. The peak heavy particle temperature, as seen in Figs. 6g–j, remains fairly constant at approximately 23,000 K, whereas the peak vibrational-electronic temperature decreases from 10,000 to 8500 K. The thermal profile begins to precede the rise in electron number density, which begins to decline in magnitude, as well as flattening in profile on this logorithmic scale. Significant flattening of the profile will diminish the accuracy of the distance measurement if the critical number density is on the plateau of the curve. The electron number density profiles begin to lose their high peak in the immediate postshock region as the region of nonequilibrium flow increases and diffuses the definition of the thermal peaks.

Conclusions

A parametric variation of thermochemical nonequilibrium models for reaction rates, translational and vibrational-electronic energy exchange rates, and the average electronic excitation level of atoms is conducted to show how MRIS measurements may be used to critically evaluate and improve kinetic models for use in hypersonic, thermochemical nonequilibrium flow simulations. The parametric study, implemented with Program LAURA, reveals a particular sensitivity of the onset and severity of an electron avalanche phenomena associated with changes in these physical models. The distinction between axisymmetric and three-dimensional models is minor. This and similar studies could well be done by axisymmetric methods to reduce computational effort.

Parametric variations of average atomic ionization potentials, which model electron energy loss in the process of electron impact ionization, showed relatively small effects on the electron number density profile for the baseline case. Significant differences in the kinetic rates for electron-impact ionization in the Kang and Dunn and Park model yield correspondingly large differences in the magnitude and location of the peak electron number density in the shock layer. The Kang and Dunn model predicts a more severe electron avalanche phenomena in the shock layer than the Park model for the baseline case. Models that enhance translational and vibrational-electronic energy exchange in the two-temperature model tend to increase ionization levels in the shock layer.

A sample AFE trajectory spanning from 70 seconds after entry interface to 250 seconds after entry interface tracks the evolution of the electron number density, translational temperature, and vibrational-electonic temperature profiles. The maximum electron number density moves from the boundary-layer edge early in the trajectory when electron-impact ionization is important to a few centimeters behind the bow shock late in the trajectory. Peak electron number density decreases by about a factor of 50 over this time.

The MRIS experiment provides the only nonintrusive profile characterization of the flowfield surrounding the AFE, which shows sensitivity to the details of the physical models. It cannot be used in and of itself to validate any single kinetic model used in the simulation because of the interactions of many uncertainties in the kinetic models, only some of which have been considered here. Errors in one aspect of the modeling may compensate for errors made in some other aspect. It is unlikely that such compensation will exactly balance over an entire trajectory, but even this possibility cannot yet be ruled out. However, the code validation process requires several different kinds of measurements that exhibit sensitivity to unknowns in the physical modeling. The ability of the MRIS experiment to contribute one such set of data is established.

Acknowledgments

The preceding study was sponsored in part by NASA Contract NAS1-19237. The authors wish to thank the Technical Monitor, Mr. David Throckmorton, for his support.

References

[1]Jones, J. J., "The Rationale for an Aeroassist Flight Experiment," AIAA Paper 87-1508, June 1987.

[2]Neece, R. T., and Marshall, R. E., "A Space Shuttle Deployed Four Frequency Millimeter Wave Radar for Measuring Electron Density Profiles in Geosynchronous Reentry Plasma," *International Union of Radio Science Symposium Digest,* University of Western Ontario, Canada, June 24–28, 1991, p. 609.

[3]Ybarra, G. A., Adralan, S. H., Hearn, C. P., Marshall, R. E., and Neece, R. T., "Detection of Target Distance in the Presence of an Interfering Reflection Using a Frequency Stepped Double Sideband Suppressed Carrier Microwave Radar System," *IEEE Transactions on Microwave Theory and Techniques,* Vol. 39, No. 5, May 1991, pp. 809–818.

[4]Park, C., "The Assessment of Two-Temperature Kinetic Model for Ionizing Air," AIAA Paper 87-1574, June 1987.

[5]Park, C., "A Review of Reaction Rates in High Temperature Air," AIAA Paper 89-1740, June 1989.

[6]Park, C., *Nonequilibrium Hypersonic Aerothermodynamics,* Wiley, New York, 1990.

[7]Kang, S. W., and Dunn, M. G., "Theoretical and Measured Electron Density Distributions for the RAM Vehicle at High Altitudes," AIAA Paper 72-689, June 1972.

[8]Gnoffo, P. A., Gupta, R. N., and Shinn, J., "Conservation Equations and Physical Models for Hypersonic Air Flows in Thermal and Chemical Nonequilibrium," NASA TP 2867, 1989.

[9]Gnoffo, P. A., "Upwind-Biased, Point-Implicit Relaxation Strategies for Viscous, Hypersonic Flows," AIAA Paper 89-1972, June 1989.

[10]Roe, P. L., "Approximate Riemann Solvers, Parameter Vectors, and Difference Schemes," *Journal of Computational Physics,* Vol. 43, No. 2, 1981, pp. 357–372.

[11]Harten, A., "High Resolution Schemes for Hyperbolic Conservation Laws," *Journal of Computational Physics,* Vol. 49, No. 3, 1983, pp. 357–393.

[12]Yee, H. C., "On Symmetric and Upwind TVD Schemes," NASA TM 86842, Sept. 1985.

[13]Yee, H. C., "Numerical Experiments with a Symmetric High-Resolution Shock-Capturing Scheme," NASA TM 88325, June 1986.

[14]Kolodziej, P., and Stewart, D. A., "Nitrogen Recombination on High-Temperature Reusable Surface Insulation and the Analysis of Its Effect on Surface Catalysis," AIAA Paper 87-1637, June 1987.

[15]Gupta, R. N., Yos, J. M., Thompson, R. A., and Lee, K. P., "A Review of Reaction Rates and Thermodynamic and Transport Properties for an 11-Species Air Model for Chemical and Thermal Nonequilibrium Calculations to 30,000 K," NASA RP 1232, Aug. 1990.

[16]Hansen, C. F., "Collision-Induced Gas Phase Dissociation Rates," Final Rept. on NASA Grant NAG1-1046, Aug. 1990.

Michael E. Tauber
Associate Editor